Nanoelectronics and Its New Materials – A NEW ERA OF NANOSCIENCE

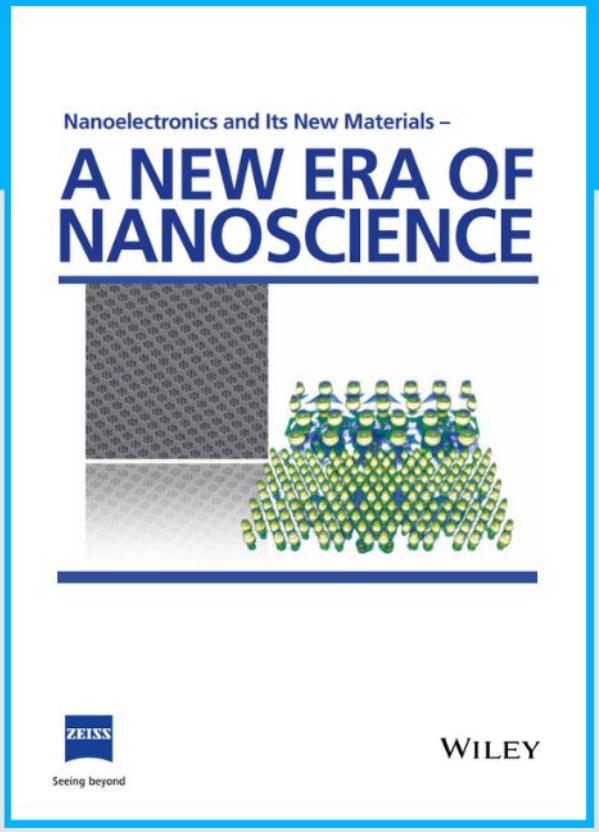

Discover the recent advances in electronics research and fundamental nanoscience.

Nanotechnology has become the driving force behind breakthroughs in engineering, materials science, physics, chemistry, and biological sciences. In this compendium, we delve into a wide range of novel applications that highlight recent advances in electronics research and fundamental nanoscience. From surface analysis and defect detection to tailored optical functionality and transparent nanowire electrodes, this eBook covers key topics that will revolutionize the future of electronics.

To get your hands on this valuable resource and unleash the power of nanotechnology, simply download the eBook now. Stay ahead of the curve and embrace the future of electronics with nanoscience as your guide.

ZEISS

Seeing beyond

WILEY

Check for updates

NANO · MICRO small
www.small-journal.com

Porous Host–Guest MOF-Semiconductor Hybrid with Multisites Heterojunctions and Modulable Electronic Band for Selective Photocatalytic CO_2 Conversion and H_2 Evolution

Tianxi Zhang, Fanlu Meng, Minmin Gao, Jishi Wei, Kane Jian Hong Lim, Kang Hui Lim, Prae Chirawatkul, Andrew See Weng Wong, Sibudjing Kawi, and Ghim Wei Ho**

Optimizing catalysts for competitive photocatalytic reactions demand individually tailored band structure as well as intertwined interactions of light absorption, reaction activity, mass, and charge transport. Here, a nanoparticulate host–guest structure is rationally designed that can exclusively fulfil and ideally control the aforestated uncompromising requisites for catalytic reactions. The all-inclusive model catalyst consists of porous Co_3O_4 host and $Zn_xCd_{1-x}S$ guest with controllable physicochemical properties enabled by self-assembled hybrid structure and continuously amenable band gap. The effective porous topology nanoassembly, both at the exterior and the interior pores of a porous metal–organic framework (MOF), maximizes spatially immobilized semiconductor nanoparticles toward high utilization of particulate heterojunctions for vital charge and reactant transfer. In conjunction, the zinc constituent band engineering is found to regulate the light/molecules absorption, band structure, and specific reaction intermediates energy to attain high photocatalytic CO_2 reduction selectivity. The optimal catalyst exhibits a H_2-generation rate up to 6720 µmol g^{-1} h^{-1} and a CO production rate of 19.3 µmol g^{-1} h^{-1}. These findings provide insight into the design of discrete host–guest MOF-semiconductor hybrid system with readily modulated band structures and well-constructed heterojunctions for selective solar-to-chemical conversion.

1. Introduction

With the worsening environmental problems and energy crisis, the exploitation and conversion of renewable solar energy have attracted tremendous attention.[1–3] Greenhouse effects, resulting from the voluminous emission of carbon dioxide and methane, would be remediated by means of CO_2 capture, storage, and utilization technology.[4,5] In addition, hydrogen energy, with the advantage of high caloric value and inhibition of greenhouse gas and pollution production during the utilization process, is considered a promising alternative energy to replace the traditional fossil fuels.[6–10] Currently, photocatalysis has been a promising strategy due to its ability to realize both CO_2 conversion to value-added fuels and H_2 production via renewable solar energy without external energy input.[11–13] However, there is a competitive reaction between photocatalytic CO_2 conversion and H_2 production, since both reactions rest upon electrons to convert CO_2 to value-added fuels or reduce water

T. Zhang, K. H. Lim, S. Kawi
Department of Chemical & Biomolecular Engineering
National University of Singapore
4 Engineering Drive 4, Singapore 117585, Singapore
E-mail: chekawis@nus.edu.sg

F. Meng, M. Gao, J. Wei, K. J. H. Lim, G. W. Ho
Department of Electrical and Computer Engineering
National University of Singapore
4 Engineering Drive 3, Singapore 117583, Singapore
E-mail: elehgw@nus.edu.sg

P. Chirawatkul
Synchrotron Light Research Institute (Public Organization)
111 University Avenue
Muang, Nakhon Ratchasima 30000, Thailand

A. S. W. Wong
Facility for Analysis Characterization Testing and Simulation (FACTS)
Nanyang Technological University
Singapore 639798, Singapore

G. W. Ho
Institute of Materials Research and Engineering
A*STAR (Agency for Science, Technology and Research)
3 Research Link, Singapore 117602, Singapore

The ORCID identification number(s) for the author(s) of this article can be found under https://doi.org/10.1002/smll.202301121

© 2023 The Authors. Small published by Wiley-VCH GmbH. This is an open access article under the terms of the Creative Commons Attribution License, which permits use, distribution and reproduction in any medium, provided the original work is properly cited.

DOI: 10.1002/smll.202301121

to H_2.[14,15] Therefore, it is imperative to develop an explicit catalyst that can fulfil simultaneous CO_2 reduction reactions and H_2 production. Concurrently, conceiving such a catalyst facilitates one to controllably regulate specific reaction parameters through studying the relationship between catalysts design and reaction paths.

A solid solution, different from the simple physical mixing of two specific components, is a typical single crystal structure with a range of compositions.[16,17] It is an ideal photocatalyst material to study the reaction control in which the electronic structure can be adeptly and continuously modulated without crystal phase transformation.[18,19] Among them, ZnCdS solid solution is considered a suitable candidate for both photocatalytic CO_2 conversion and H_2 evolution due to its well-matched band structure, excellent light absorption, and electrical conductivity.[20–23] However, work on revealing the reaction pathway control of CO_2 conversion and H_2 production is still deficient. Meanwhile, the unmodified ZnCdS solid solution still suffers from serious photocorrosion and high recombination rate of electrons and holes problems,[24,25] which further limits their wide application in the photocatalysis field.

Metal–organic frameworks (MOFs), a fascinating class of porous materials, have attracted significant interest in a variety of applications due to their high surface area, unique porous construct, and readily functionalize structure.[26–29] The integration of MOFs with traditional semiconductor-based photocatalysts enables rational design and fine tuning of the heterojunction at a molecular level via the metal clusters and bridging organic linkers.[30–32] Three-dimensional (3D) cyanide coordination MOFs, typically known as Prussian blue analogs (PBAs) with intrinsic porosity allow assembly of another catalyst, have been reported in the field of catalysis.[33,34] Particularly, PBA-derived Co_3O_4 porous framework is one promising candidate to integrate with semiconductor for bifunctional photocatalytic CO_2 conversion reaction[35–37] and H_2 evolution. Above all, effective porous topology nanoassembly, not just on the exterior but more importantly into the interior pores of a porous matrix, signifies the key attribute to improve the efficiency of heterogeneous junction formation in the context of creating and exposing abundant nanoparticulate interfaces to the greatest extent. Notably, this strategy is crucial to improve charge transfer occurring predominantly at the interface. In conjunction, aggregation and leaching of catalysts, leading to loss of catalytic activity and recyclability can be circumvented. However, establishing such porous nanoassembly has proven to be markedly challenging owing to high capillary tension and ill-fitted pores geometry. Furthermore, limited works are focused on porous host–guest MOF-semiconductor hybrid system with distinct nanoassembly and modulable electronic band of a discrete catalyst design that exhibits remarkable catalytic activity and selectivity for dual photocatalytic CO_2 conversion and H_2 evolution.

Here, we report the design of a particulate host–guest MOF-semiconductor hybrid system for competitive photocatalytic reactions with controllable band structure and favorable light absorption, reaction activity, mass, and charge transport determinants. The spontaneously assembled nanoparticulate host–guest scheme facilitates the dispersion and immobilization of nanoparticle guest onto 3D porous host to significantly increase heterojunction to afford high density stably confined active sites (**Figure 1**). Moreover, the coupling of a continuously modulated $Zn_xCd_{1-x}S$ solid solution guest of amenable electronic structure with PBAs derived Co_3O_4 porous host effectively controls the reaction pathway for competitive photocatalytic reactivity (Figure 1). Due to the characteristic of solid solution, the energy band structure, light absorption, and photocatalytic activity can be regulated by simply adjusting the metal additive concentration to selectively target the photocatalytic CO_2 reduction reaction or H_2 evolution. Complementary simulation and experimental characterizations were then employed to study the relationship between the composition of ZnCdS solid solution and reaction control of photocatalytic CO_2 reduction and competitive H_2 production. These findings provide insight into high efficiency nanoassembly of nanoparticulate heterojunction that offers a unique opportunity to maximize active sites and improve activity, selectivity, and stability of a heterogeneous catalyst.

2. Results and Discussion

Porous Co_3O_4 host was first prepared to serve as the framework to load $Zn_xCd_{1-x}S$ guest and form multisites heterojunctions with $Zn_xCd_{1-x}S$. Co–Co PBA nanocubes (the chemical formula is $Co_3[Co(CN)_6]_2$) with transition metal ions bridged by cyano ligands) were synthesized by the typical coprecipitation method and were then transformed into Co_3O_4 after subsequent calcination in air. Due to the spontaneous contraction of Co_3O_4 during the calcination process, the surface of shrunken Co_3O_4 nanoboxes is much rougher, compared with the smooth cube-like structure with a solid internal feature of Co–Co PBA (Figures S1 and S2, Supporting Information). Consequently, the Co_3O_4 nanoboxes composed of numerous particles will advantageously provide plentiful pores between the nanograins junction to load $Zn_xCd_{1-x}S$ nanoparticles. The SEM images in **Figure 2**a show that $Zn_xCd_{1-x}S/Co_3O_4$ composite exhibit uniform nanocubes with a rough surface. The distribution of $Zn_xCd_{1-x}S$ nanoparticles (green circles in Figure 2c,e,f) can be clearly observed from the representative TEM and energy-dispersive X-ray (EDX) mapping images of $Zn_{0.5}Cd_{0.5}S/Co_3O_4$ composites (Figure 2b–g). In Figure 2b,c, it proved the porous structure of Co_3O_4 host and ZnCdS guest nanoparticles are well-dispersed both on the surface and in the cavity of Co_3O_4. This kind of effective assembly of ZnCdS on both the exterior and interior pores of Co_3O_4 matrix will stably immobilize abundant nanoparticles that form intercontact structure, which will significantly create and expose multisites heterojunctions, beneficial for mass and charge transfer. A magnified view at the edge of $Zn_{0.5}Cd_{0.5}S/Co_3O_4$ composites evidently shows the distribution of ZnCdS nanoparticles on the surface of Co_3O_4 framework (Figure 2d). Additionally, the surface of a single Co_3O_4 is surrounded by several ZnCdS nanoparticles, forming a high density of heterojunctions (Figure 2e). The high-resolution TEM (HRTEM) images of $Zn_{0.5}Cd_{0.5}S/Co_3O_4$ composites display lattice fringes of 0.33 nm corresponding to the (002) crystal facet of a solid solution of $Zn_{0.5}Cd_{0.5}S$, with lattice fringes between that of CdS (PDF No. 41–1049) and ZnS (PDF No. 36–1450). In addition, the lattice fringe of 0.47 nm is consistent with (111) plane of Co_3O_4, which confirms the hybrid heterostructures of $Zn_{0.5}Cd_{0.5}S$ and Co_3O_4 (Figure 2f). The high-angle annular dark-field (HAADF) as well as EDX-mapping images in Figure 2g verify a homogeneous distribution of Co,

© 2023 The Authors. Small published by Wiley-VCH GmbH

16136829, 0, Downloaded from https://onlinelibrary.wiley.com/doi/10.1002/smll.202301121, Wiley Online Library on [17/09/2023]. See the Terms and Conditions (https://onlinelibrary.wiley.com/terms-and-conditions) on Wiley Online Library for rules of use; OA articles are governed by the applicable Creative Commons License

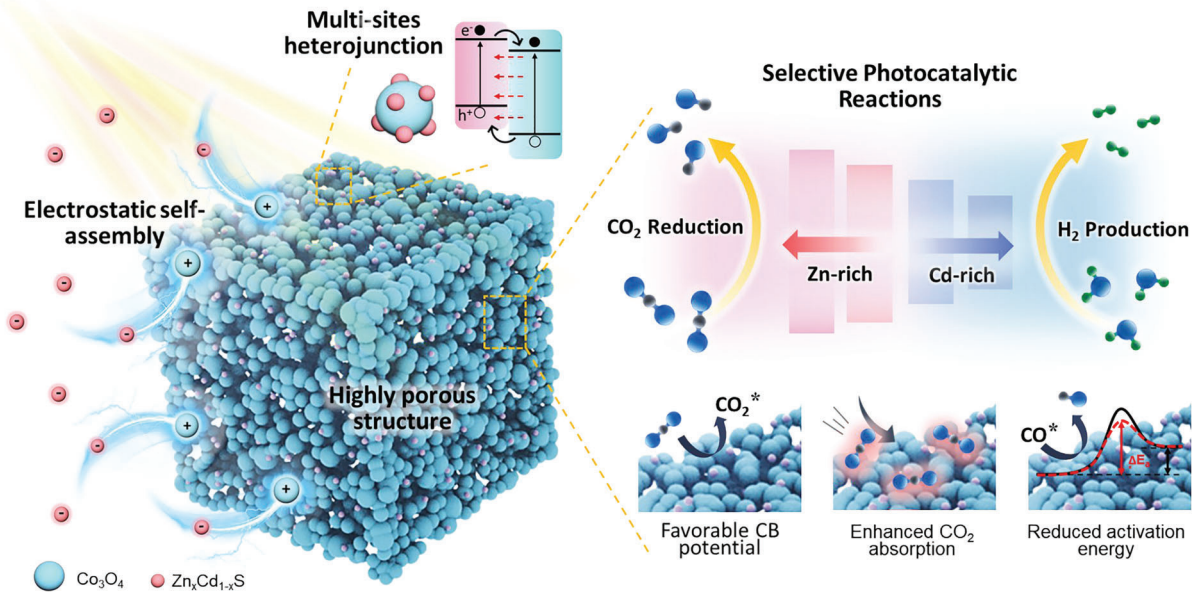

Figure 1. Schematic diagram of nanoassembly of host–guest $Co_3O_4/Zn_xCd_{1-x}S$ via porous framework and electrostatic interactions to attain controllable reaction pathway of photocatalytic CO_2 reduction and H_2 generation over multisites heterojunction.

O, Zn, Cd, and S elements. More importantly, Zn, Cd, and S elements are not only distributed on the surface of Co_3O_4, they are also well dispersed in the whole cavity of Co_3O_4, which will be advantageous for the formation of multisites heterojunction between ZnCdS nanoparticles guest and Co_3O_4 nanoboxes host.

Furthermore, the phase structure of $Zn_{0.5}Cd_{0.5}S/Co_3O_4$ composites was investigated by X-ray diffraction (XRD). It can be seen from the XRD pattern in Figure 2h that $Zn_{0.5}Cd_{0.5}S/Co_3O_4$ sample mainly exhibits all the similar peaks to $Zn_{0.5}Cd_{0.5}S$, while the other four peaks at 31.3°, 36.8°, 59.4°, and 65.2° correspond to (220), (311), (511), and (440) planes of Co_3O_4 (JCPDS Card No. 43–1003), indicating the successful dispersion of $Zn_{0.5}Cd_{0.5}S$ into the Co_3O_4 nanoboxes (Figures S3 and S4, Supporting Information). Notably, the dispersion of Co_3O_4 aqueous solution showed a positive charge state with the zeta potential of 33.7 mV, while $Zn_{0.5}Cd_{0.5}S$ solid solution in acidic solution demonstrated a remarkably negatively charged surface with a zeta potential value of –16.9 mV (Figure 2i). Therefore, the mutual electrostatic force readily realized the spontaneous self-assembly of ZnCdS solid solution guest onto Co_3O_4 nanoboxes host. The distinctive hierarchical open and porous configuration as well as electrostatic coordinated $Zn_xCd_{1-x}S/Co_3O_4$ host–guest hybrid photocatalyst endows desirable multisite heterojunctions, strong interfacial contacts, and extensive exposure of active sites to further promote the photocatalytic activity of $Zn_xCd_{1-x}S$.

Furthermore, Co_3O_4 host framework with different degrees of porous structure has been investigated to form different density of heterojunctions with $Zn_xCd_{1-x}S$ guest. Co_3O_4 host was acquired through different calcination temperature of Co–Co PBA, and it can be seen from Figure S5 (Supporting Information) that $Zn_xCd_{1-x}S/Co_3O_4$ composite labeled as CCZ_600 °C has a lower charge transfer resistance than CCZ_400 °C and CCZ_700 °C, resulting from a higher density of heterojunctions between $Zn_xCd_{1-x}S$ and Co_3O_4 framework calcinated at 600 °C. This result is due to the insufficient calcination of Co–Co PBA at 400 °C, while too high calcination temperature at 700 °C results in the collapse of the porous nanocube structure framework (Figure S6, Supporting Information). The optimal calcination temperature of 600 °C is not only able to ensure the maintenance of nanostructure scaffold but also produces plentiful pores to infiltrate ZnCdS guest, thereby forming porous host–guest MOF-semiconductor hybrid photocatalyst with multisites heterojunctions. Additionally, such porous nanoassembly of host–guest MOF-semiconductor hybrid with multisites heterojunction will produce a higher photocurrent intensity and lower charge transfer resistance of Zn_5Cd_5/porous Co_3O_4 sample compared with general Zn_5Cd_5S/Co_3O_4 nanoparticles composite (**Figure 3**a,b). These results confirm that the rational design of grafting guest nanoparticles into the exterior and interior pores of the porous matrix will improve the efficiency of heterogeneous junction, which will be beneficial for the subsequent photocatalytic reactivity.

In addition to the rational design of porous host–guest hybrid system for intertwined interactions, optimizing catalysts toward targeted photocatalytic reactions selectively is of great significance to improve the catalytic efficiency. Band structure of the MOF-semiconductor photocatalyst has been subsequently tailored for target competitive photocatalytic reactions. Due to the characteristic of solid solution, the coordinated $Zn_xCd_{1-x}S$ can be regulated by simply adjusting the metal additive concentration to obtain progressively manipulated compositions and electronic structures. ZnCdS solid solution with a range of different compositions was prepared and examined through a series of morphological, crystal, and compositional characterizations. As shown in Figure S7a–f (Supporting Information), the obtained pure CdS exhibited nanoparticle form with an average particle size of 18.8 nm. With the addition of zinc, all the samples retain nanoparticle structure without obvious morphological

 © 2023 The Authors. Small published by Wiley-VCH GmbH

16136829, 0, Downloaded from https://onlinelibrary.wiley.com/doi/10.1002/smll.202301121, Wiley Online Library on [17/09/2023]. See the Terms and Conditions (https://onlinelibrary.wiley.com/terms-and-conditions) on Wiley Online Library for rules of use; OA articles are governed by the applicable Creative Commons License

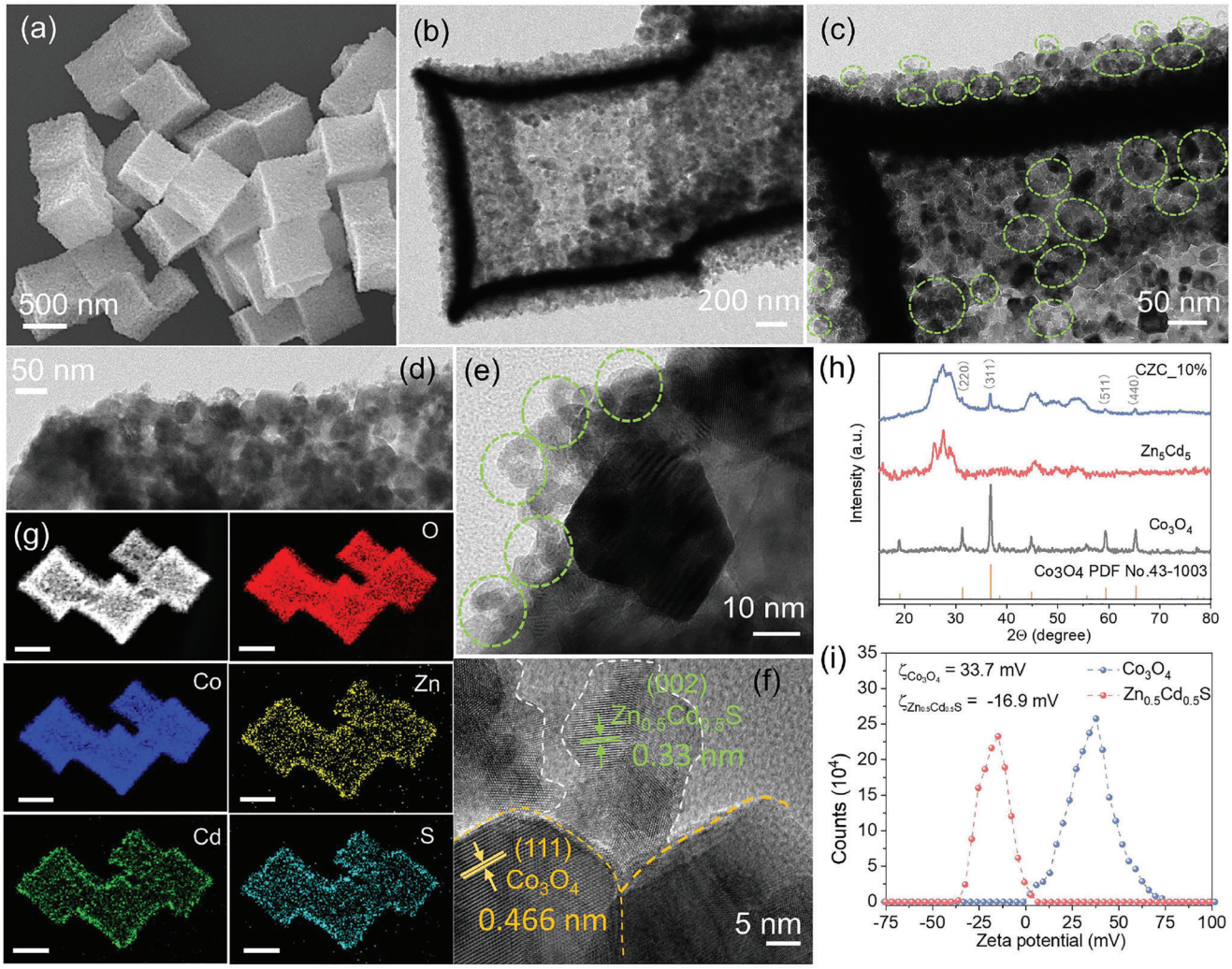

Figure 2. a) SEM image and b) TEM image of $Zn_{0.5}Cd_{0.5}S/Co_3O_4$ host–guest hybrid photocatalyst. c–e) High-magnified TEM images of $Zn_{0.5}Cd_{0.5}S/Co_3O_4$ composites. f) HRTEM image of the $Zn_{0.5}Cd_{0.5}S$ guest part and Co_3O_4 host part of $Zn_{0.5}Cd_{0.5}S/Co_3O_4$ composites (green circles in (c), (e), and (f) represent $Zn_{0.5}Cd_{0.5}S$ nanoparticles). g) HAADF image and EDX-mapping images of $Zn_{0.5}Cd_{0.5}S/Co_3O_4$ composites (scale bar: 500 nm). h) XRD patterns of $Zn_{0.5}Cd_{0.5}S$, Co_3O_4, and $Zn_{0.5}Cd_{0.5}S/Co_3O_4$ composites. i) Zeta potential profiles of $Zn_{0.5}Cd_{0.5}S$ and Co_3O_4.

transformation. The $Zn_{0.5}Cd_{0.5}S$ solid solution (Figure S8a–d, Supporting Information) has an average diameter of 13.1 nm and the lattice fringes of 0.33 nm, well corresponded to the (002) crystal facet of $Zn_{0.5}Cd_{0.5}S$. However, due to the relatively small atomic radius of zinc, the average diameter of ZnCdS solid solution is observed to decrease from 18.8 to 10.2 nm with increasing zinc atoms content (Table S1, Supporting Information). These morphological characterizations of ZnCdS solid solution confirmed the successful synthesis of $Zn_xCd_{1-x}S$ with different compositions by simply adjusting the metal additive concentration.

It is essential for ZnCdS solid solution with one single crystal structure (cocrystal) to be formed instead of a mixture of multicomponents. The formation of cocrystal with homogenous lattice offers more predictable engineering of electronic band structure as the packing motif is largely undisturbed by compositional variation. The phase and crystal structure of the ZnCdS solid solution were then investigated by XRD and the results were shown in Figure 3c. Compared with pure CdS (PDF No. 41–1049) and ZnS (PDF No. 36–1450), it is found that the diffraction peaks of $Zn_xCd_{1-x}S$ would continuously shift from CdS toward a higher angle of ZnS when more Zn was added. These peaks correspond to (100), (002), (101), (110), (103), and (112) crystal planes of $Zn_xCd_{1-x}S$. All the peaks are located between CdS and ZnS diffraction without obvious impurities. These results indicated the zinc atoms are incorporated into the CdS lattice to successfully form $Zn_xCd_{1-x}S$ solid solution, consistent with the HRTEM results. Apart from the single crystallinity, the actual ratio between Zn and Cd in the synthesized ZnCdS solid solution also plays a vital role in the subsequent catalysis reactions. Thereafter, EDS and X-ray photoelectron spectroscopy (XPS) were performed to investigate the composition of ZnCdS solid solution. Figure S9 (Supporting Information) exhibited the elemental distribution of $Zn_{0.5}Cd_{0.5}S$ sample and the acquired atomic molar percentage of Zn was calculated as 50%, which closely matches the precursor molar ratio (Table S2, Supporting Information).

 © 2023 The Authors. Small published by Wiley-VCH GmbH

16136829, 0, Downloaded from https://onlinelibrary.wiley.com/doi/10.1002/smll.202301121, Wiley Online Library on [17/09/2023]. See the Terms and Conditions (https://onlinelibrary.wiley.com/terms-and-conditions) on Wiley Online Library for rules of use; OA articles are governed by the applicable Creative Commons License

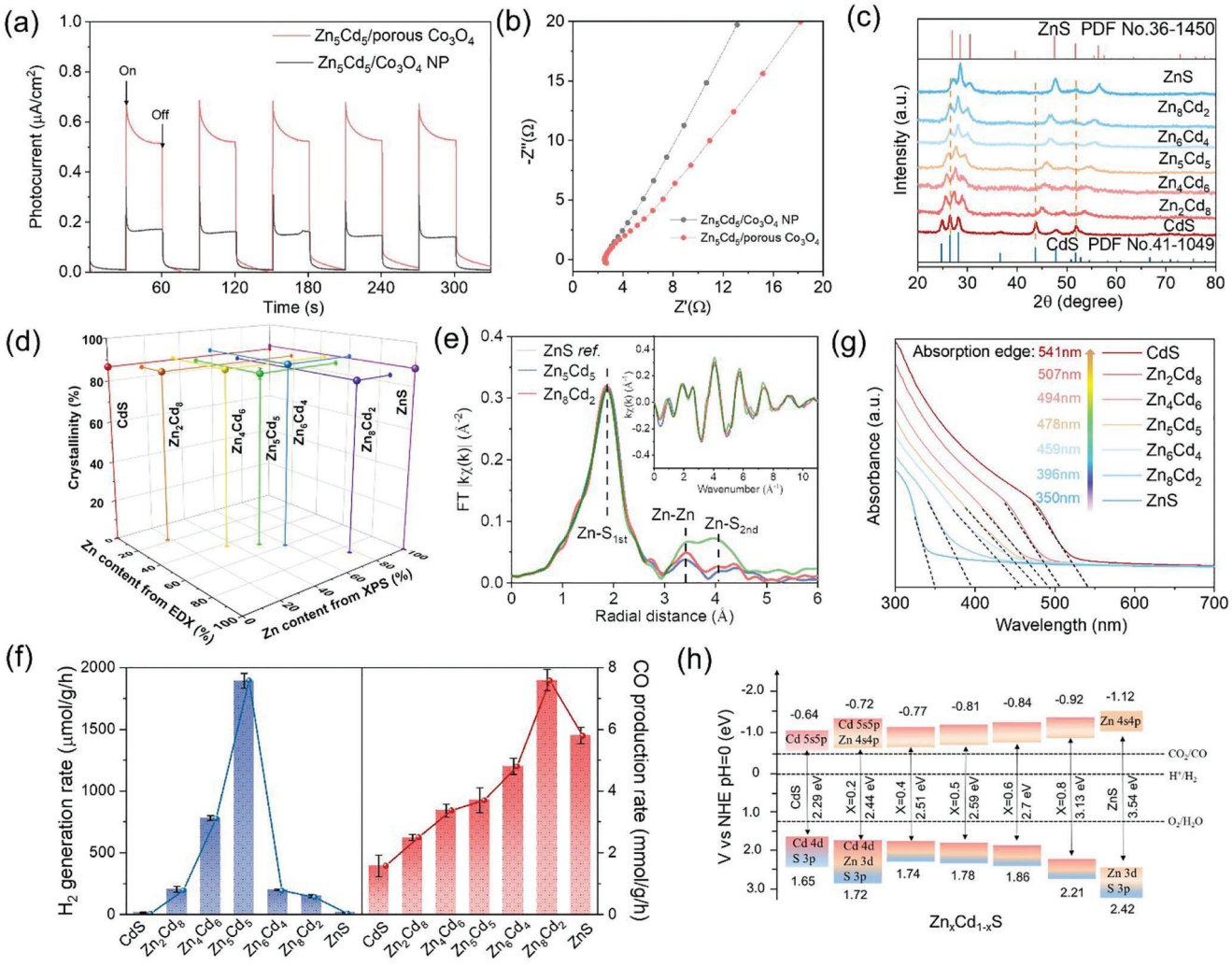

Figure 3. a) Photocurrent response and b) Nyquist plots comparison of $Zn_{0.5}Cd_{0.5}S/Co_3O_4$ multisites heterojunction and $Zn_{0.5}Cd_{0.5}S/Co_3O_4$ nanoparticles heterojunction. c) XRD patterns of ZnCdS solid solution with different molar ratios of Zn and Cd. d) Zn content calculation based on EDX and XPS results, and crystallinity of ZnCdS solid solution with different Zn/Cd molar ratios. e) The Zn K-edge of corresponding FT-space spectra converted from k-space, and k1-weighted EXAFS spectra (insert images) of $Zn_{0.5}Cd_{0.5}S$ and $Zn_{0.8}Cd_{0.2}S$. f) Average photocatalytic H_2-evolution and CO_2 reduction performance comparison of ZnCdS solid solution with the different molar ratio of Zn and Cd. g) UV–vis absorption spectra of $Zn_xCd_{1-x}S$ samples. h) Band structures of $Zn_xCd_{1-x}S$ samples.

Furthermore, when more zinc atoms were introduced, the peak area of zinc substantially increased while cadmium dropped as seen from the XPS analysis in Figure S10 and Table S3 (Supporting Information). The atomic proportions based on EDX and XPS results and crystallinity of ZnCdS solid solution were shown in Figure 3d. It shows that the prepared solid solution samples have a similar crystallinity of around 85% and the actual Zn content was consistent with the precursor ratio. All these results indicated the success of continuous modulation of ZnCdS solid solution with successive compositions, which is essential for the following studies on the relationships between the zinc constituent band engineering and optimized photocatalytic reactions paths.

Although XRD results have demonstrated the single crystal phase of solid solution, extended X-ray absorption fine structure (EXAFS) is further studied to reveal the structural information with respect to zinc concerning the neighboring atoms and coordination number. Figure 3e and Figure S11 (Supporting Information) show the Zn K-edge of representative $Zn_{0.5}Cd_{0.5}S$ and $Zn_{0.8}Cd_{0.2}S$ samples. The strong peak at around 2.0 Å was observed in the Fourier transform (FT) of the Zn K-edge EXAFS spectrum, corresponding to the Zn–S bond in the first shell scattering. Another strong peak at around 3.2 Å was assigned to Zn–Zn bond, indicating the second shell of neighboring Zn around Zn atoms.[38,39] Due to the existence of Zn–Cd bonds in the solid solution, the intensity of Zn–Zn peaks over $Zn_{0.5}Cd_{0.5}S$ and $Zn_{0.8}Cd_{0.2}S$ samples is lower than that of ZnS reference sample. The intensity drops significantly with the decreasing amount of Zn atoms. This phenomenon demonstrated the formation of well-defined ZnCdS solution rather than a mixture of separate CdS and ZnS phases, further excluding the concerning about the difference between the activity property of $Zn_{0.5}Cd_{0.5}S$ and $Zn_{0.8}Cd_{0.2}S$ samples is attributed to the different crystal structure.

© 2023 The Authors. Small published by Wiley-VCH GmbH

16136829, 0, Downloaded from https://onlinelibrary.wiley.com/doi/10.1002/smll.202301121, Wiley Online Library on [17/09/2023]. See the Terms and Conditions (https://onlinelibrary.wiley.com/terms-and-conditions) on Wiley Online Library for rules of use; OA articles are governed by the applicable Creative Commons License

The above morphological structures, phase composition, and coordination information of ZnCdS solid solution confirmed the successful modulation of $Zn_xCd_{1-x}S$ with different compositions by simply adjusting the metal additive concentration. Interestingly, completely different stoichiometries of $Zn_xCd_{1-x}S$ samples are judiciously tuned to achieve the optimal photocatalytic CO_2 reduction rate and water-splitting reactions. As shown in Figure 3f, CdS showed a relatively low H_2 production rate of 15 μmol g^{-1} h^{-1} compared with solid solutions cocrystals. When more zinc precursors were introduced, $Zn_{0.5}Cd_{0.5}S$ exhibited the highest H_2 evolution rate, which could reach up to 1893 μmol g^{-1} h^{-1}. However, the H_2 evolution would drop dramatically with a further increase in zinc content. This result was consistent with the previous report on $Zn_xCd_{1-x}S$ solid solutions for photocatalytic water splitting.[40] The constituent effect of $Zn_xCd_{1-x}S$ solid solutions was also extended to the photocatalytic CO_2 reduction reactions. Similarly, the solid solutions cocrystals present an improved CO production rate compared with pristine CdS. However, it was uncovered that $Zn_{0.8}Cd_{0.2}S$ cocrystal achieves the optimal photocatalytic CO_2 reduction rate unlike a different stoichiometry of $Zn_{0.5}Cd_{0.5}S$ in the context of water-splitting reactions (Figure 3f and Figure S12, Supporting Information). The significantly increase in zinc atom is desired for CO_2 reduction process, indicating the disparate course of reaction between photocatalytic H_2 generation and CO_2 reduction process, aside from the consistent provision of efficient light absorption and electrons charge transfer.

To reveal the relationship between the compositional engineering of ZnCdS solid solution and reaction control of selective CO_2 conversion and competitive H_2 production, a series of experimental characterizations and complementary simulation were subsequently employed. Through such kind of compositional tuning, the light absorption capacity of $Zn_xCd_{1-x}S$ catalyst will be regulated, which is one crucial factor for photocatalytic performance. As illustrated in Figure 3g, pure CdS exhibits an excellent visible light absorption property with the absorption edge at 541 nm, corresponding to a bandgap of 2.29 eV. In contrast, bare ZnS could only absorb UV light with the bandgap of 3.54 eV.[41] As for $Zn_xCd_{1-x}S$ cocrystal, the color would gradually change from pale white to bright yellow (Figure S13, Supporting Information) and correspondingly the absorption edge would red-shift to the visible light region with the reduced zinc content. However, CdS sample shows an excellent light absorption property, it is neither the optimal catalyst for photocatalytic CO_2 conversion nor competitive H_2 production, indicating the light absorption is not the dominant factor for such photocatalytic CO_2 reduction and H_2 evolution process.

Obviously, an elevated overpotential difference between the conduction band (CB) bottom and the required potential for a particular reaction is favorable for photocatalytic redox reactions, including CO_2 reduction and H_2 production. Typically, CB bottom potential of $Zn_xCd_{1-x}S$ is formed through the hybridized (Cd 5s5p + Zn 4s4p) orbitals and thereby the bandgap of $Zn_xCd_{1-x}S$ solid solution is higher than CdS but lower than pure ZnS. Figure 3h shows the CB level that is determined based on Mott–Schottky plots and the VB level, which was then calculated based on the equation: $E_{VB} = E_{CB} + E_g$. It can be seen that CB and VB of original CdS were found to be only –0.64 and 1.65 eV, respectively. The CB and VB level of $Zn_xCd_{1-x}S$ would gradually elevate deriving from the contribution of the electronic structure of Zn (Figure S14, Supporting Information). This result was also verified by the small binding energy range scan of VB-XPS in Figure S15 (Supporting Information). The position of VB maximum (VBM) was evaluated by linearly extrapolating the onset of XPS valence band spectra to the baseline, which reflects a band-edge position with respect to Fermi level (E_f).[42,43] The VBM edge levels of CdS and ZnS were determined to be 1.41 and 2.19 eV, respectively, which shifted around 0.2–0.3 eV compared with the VB levels calculated from Mott–Schottky and bandgap. Similarly, VB of $Zn_xCd_{1-x}S$ solid solution samples also exhibited an upshift trend when x increased from 0 to 1. This mid-gap state would essentially broaden the bandgap with an enhanced redox capability of $Zn_xCd_{1-x}S$. Compared with H_2-generation reaction, photocatalytic CO_2 reduction requires a higher CB potential of –0.53 eV to overcome the reaction barrier between CO_2 and CO. As a result, the optimal sample for CO_2 reduction stipulates a higher zinc concentration and the electronic structure of $Zn_{0.8}Cd_{0.2}S$ sample is altered to realize a compatible CB level and light-harvesting capability and thus achieve the optimized CO_2 conversion performance.

Different from liquid/solid interfacial reactions of H_2 evolution, photocatalytic CO_2 reduction generally involves CO_2 gas. Therefore, apart from the light absorption and the required potential difference, the adsorption and activation of CO_2 are crucial for the subsequent reactions. As demonstrated in the CO_2 temperature-programmed desorption (TPD) profiles (**Figure 4**a), CO_2 desorption in the low-temperature range of 50–300 °C of ZnS was obviously higher than CdS, which was attributed to the hydroxyl groups in the surface. At a higher temperature of 429.6 °C, the basicity sites are stronger and generally attributed to the low coordination sites. From the intensity signal, it suggests that ZnS has a stronger CO_2 adsorption capability compared with CdS, which is an essential determining factor that $Zn_{0.8}Cd_{0.2}S$ achieves a better photocatalytic CO_2 reduction performance than $Zn_{0.5}Cd_{0.5}S$. To further investigate the specific effects of different metal species compositions on the photoreduction CO_2 reaction, density functional theory (DFT) calculations were performed. The adsorption in atomic model is shown in Figure S16 (Supporting Information) and Gibbs free energy pathways and intermediates over $Zn_{0.8}Cd_{0.2}S$ and $Zn_{0.5}Cd_{0.5}S$ are shown in Figure 4b. In the four elementary steps, $Zn_{0.8}Cd_{0.2}S$ exhibited a stronger CO_2 adsorption capacity due to a lower ΔG of 0.09 eV as compared with $Zn_{0.5}Cd_{0.5}S$ with ΔG of 0.12 eV, consistent with the experimental CO_2-TPD results. Afterward, CO_2 molecules accept one electron to form COOH*, and then produce CO*, which is the rate-determining step for photocatalytic CO_2 reduction.[44] The energy barrier of $Zn_{0.8}Cd_{0.2}S$ is 0.37 eV that was noticeably lower than $Zn_{0.5}Cd_{0.5}S$ (0.56 eV), suggesting a more favorable photoreduction reaction over $Zn_{0.8}Cd_{0.2}S$. By contrast, the free energy barrier of $Zn_{0.8}Cd_{0.2}S$ for H_2 evolution reaction (HER) is 0.365 eV as opposed to $Zn_{0.5}Cd_{0.5}S$ of 0.188 eV (Figure 4c). The considerably reduced reaction barrier of $Zn_{0.5}Cd_{0.5}S$ manifested in its readiness of HER process. It can be seen from the above analysis that CO_2 reduction process requires a higher conductive band potential, an appropriate capability between CB level and light harvesting, a stronger CO_2 adsorption and activation ability, compared with H_2 evolution reaction. Through this simple and direct composition engineering, the electronic structure of a

© 2023 The Authors. Small published by Wiley-VCH GmbH

16136829, 0, Downloaded from https://onlinelibrary.wiley.com/doi/10.1002/smll.202301121, Wiley Online Library on [17/09/2023]. See the Terms and Conditions (https://onlinelibrary.wiley.com/terms-and-conditions) on Wiley Online Library for rules of use; OA articles are governed by the applicable Creative Commons License

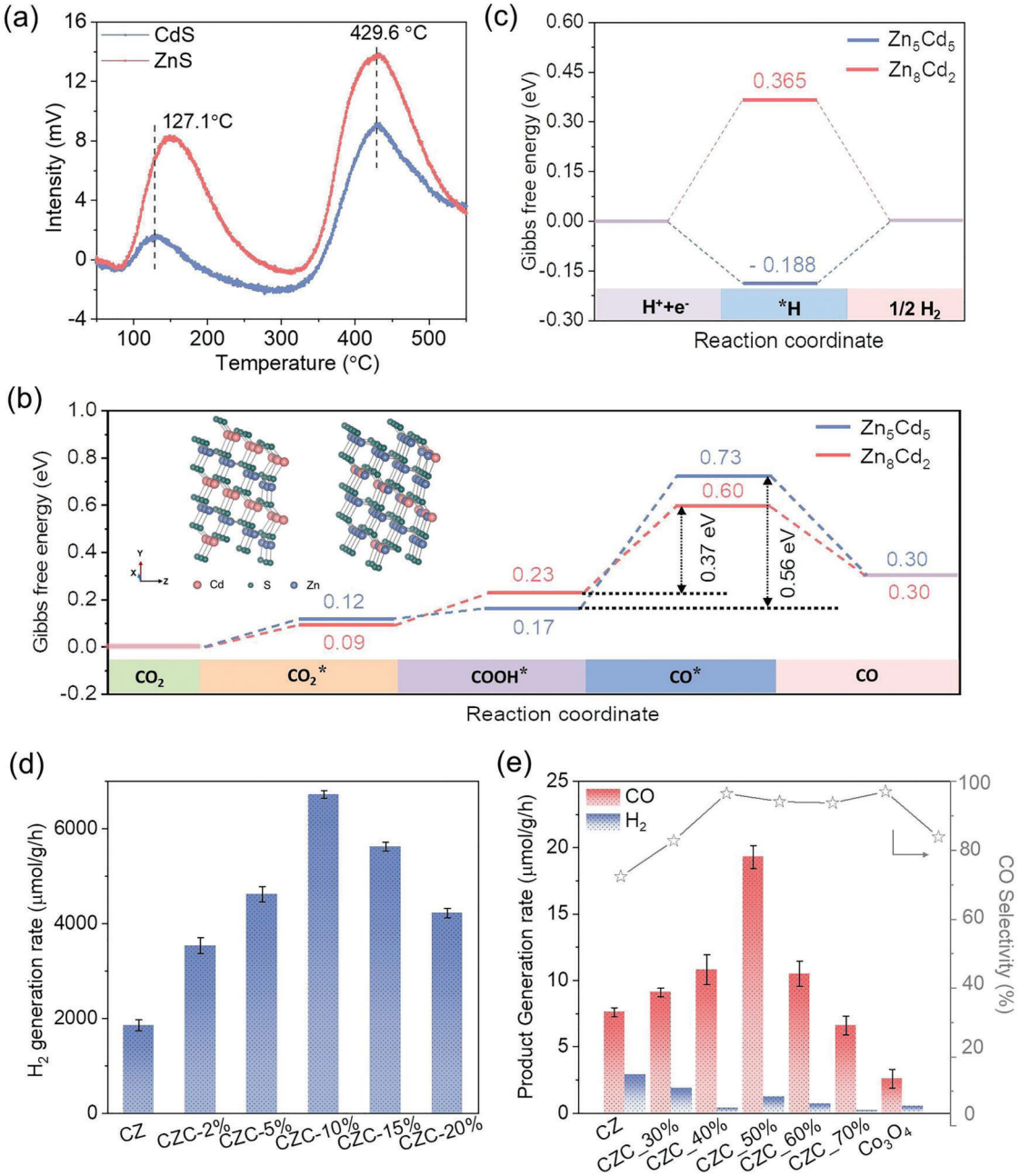

Figure 4. a) CO_2-TPD profiles of CdS and ZnS samples. b) Free energy diagram profiles for CO_2 conversion to CO, and c) free energy diagram profiles for H_2 evolutionover $Zn_{0.5}Cd_{0.5}S$ (blue) and $Zn_{0.8}Cd_{0.2}S$ (red) samples. d) Average photocatalytic H_2-evolution activity of $Zn_{0.5}Cd_{0.5}S@Co_3O_4$ composites with different loading amount of Co_3O_4. e) Average photocatalytic CO production rate and CO selectivity of $Zn_{0.8}Cd_{0.2}S@Co_3O_4$ composites with different loading amount of Co_3O_4 (CZC_x% represents $Co_3O_4/Zn_xCd_{1-x}S$ composites with x% loading amount of Co_3O_4).

catalyst can be progressively modulated, and the reaction path can be controlled toward targeted photocatalytic reactivity.

Having obtained the electrostatic coordinated $Zn_xCd_{1-x}S/Co_3O_4$ host–guest hybrid photocatalyst and the optimal catalysts for target reactions, photocatalytic CO_2 reduction and H_2 production performance of $Zn_xCd_{1-x}S/Co_3O_4$ were then evaluated under irradiation. For comparison, $Zn_xCd_{1-x}S/Co_3O_4$ samples with different loading amount of Co_3O_4 were tested. It is apparent that HER production rate gradually enhanced with increased amount of Co_3O_4 from 3536 μmol g^{-1} h^{-1} for CZC_2% to 4616 μmol g^{-1} h^{-1} for CZC_5% (CZC_x% represents $Co_3O_4/Zn_xCd_{1-x}S$ composites with x% loading amount of Co_3O_4). It reaches the highest rate of 6720 μmol g^{-1} h^{-1} for CZC_10%, which was roughly 3.6 times higher than that of the original $Zn_{0.5}Cd_{0.5}S$ (Figure 4d; Figure S17 and Table S4, Supporting Information). However, a higher loading of Co_3O_4 would inversely result in insufficient photogeneration of charge carriers, which leads to limited charge transfer and separation,

© 2023 The Authors. Small published by Wiley-VCH GmbH

16136829, 0, Downloaded from https://onlinelibrary.wiley.com/doi/10.1002/smll.202301121, Wiley Online Library on [17/09/2023]. See the Terms and Conditions (https://onlinelibrary.wiley.com/terms-and-conditions) on Wiley Online Library for rules of use; OA articles are governed by the applicable Creative Commons License

thereby shortening the active photo-induced electron lifetime for proton reduction.[45] As a result, both CZC_15% and CZC_20% samples showed an obvious decrease in H_2 yield. This indicates an optimal light absorption and charge carrier separation is achieved for the CZC_10% sample. Importantly, HER of the optimal CZC_10% composites sample could maintain at around 6720 μmol g^{-1} h^{-1} after a few cycles, indicating good recyclability and photostability of $Zn_{0.5}Cd_{0.5}S/Co_3O_4$ (Figure S18a, Supporting Information). For light-driven CO_2 reduction, when Co_3O_4 was introduced, H_2 production was greatly suppressed while the CO production rate reaches up to 19.3 μmol g^{-1} h^{-1} for the optimal $Zn_{0.8}Cd_{0.2}S/Co_3O_4$ sample (CZC_50%). The selectivity of CO increases to 95% when the amount of Co_3O_4 was tuned (Figure 4e). Compared with $Zn_{0.8}Cd_{0.2}S$ sample, the CO production rate of $Zn_{0.8}Cd_{0.2}S/Co_3O_4$ composites could also stabilize at around 19 μmol g^{-1} h^{-1} for five cycles (Figure S18b, Supporting Information). Besides, the ^{13}C and ^{18}O isotope-labeling experiments confirmed that CO originated from CO_2 molecules and water participated in the oxidation reaction (Figures S19 and S20, Supporting Information). All these results indicated the introduction of MOF-deriving Co_3O_4 host promotes the photocatalytic H_2 production and CO_2 reduction processes over $Zn_xCd_{1-x}S$ semiconductor guest.

The effect of specific surface area and pore size distribution on the photocatalytic performance were first studies by the Brunauer–Emmett–Teller (BET) method. Compared with pure $Zn_{0.5}Cd_{0.5}S$, the surface area of $Zn_{0.5}Cd_{0.5}S/Co_3O_4$ composites with 10% loading of Co_3O_4 increases to 85.27 m^2 g^{-1} (Figure S21, Supporting Information). Similarly, the surface area of $Zn_{0.8}Cd_{0.2}S/Co_3O_4$ composites with 50% loading of Co_3O_4 also increases to 90.33 m^2 g^{-1}. This enhanced surface area will promote the mass transfer of gas products and have a positive effect on both the photocatalytic CO_2 conversion and H_2 evolution process. However, compared with pure $Zn_xCd_{1-x}S$ sample, the surface area of $Zn_xCd_{1-x}S/Co_3O_4$ composites only increases by less than 12%, which means the surface area is not the dominant factor for the performance enhancement. In order to investigate the correlations between the augmented photocatalytic redox activity and the charge carrier transfer, the photocurrent response and electrochemical impedance spectroscopy (EIS) studies were subsequently conducted. It is clearly seen that all samples presented high sensitivity to light on–off cycles. When Co_3O_4 host was introduced, $Zn_{0.8}Cd_{0.2}S/Co_3O_4$ hybrid photocatalyst would generate a much higher photocurrent and smaller arc radius compared with the original $Zn_{0.8}Cd_{0.2}S$ (**Figure 5**a,b), due to lower charge transfer resistance of Co_3O_4 (the smallest semicircle). The higher photocurrent response and the smaller semicircle of Nyquist plots manifested greatly improved charge separation and transport kinetics, stemming from the efficient electron migration to Co_3O_4. Similarly, $Zn_{0.5}Cd_{0.5}S/Co_3O_4$ sample also showed enhanced photocurrent and lower interfacial charge migration resistance (Figure S22, Supporting Information). Fluorescence (FL) was also characterized to study the charge-separation efficiency. A lower FL intensity inferred reduced recombination of photo-generated electrons and holes, and thereby a higher charge-separation efficiency.[46] Bare $Zn_{0.5}Cd_{0.5}S$ showed a strong peak at around 470 nm due to the fast charge recombination of bandgap transition (Figure 5c). After the introduction of Co_3O_4, the fluorescence emission was significantly quenched, indicating its enhanced electron-trapping ability. This result is also supported by the time-resolved transient photoluminescence in Figure 5d. The average emission lifetime is prolonged from 4.98 ns ($Zn_{0.8}Cd_{0.2}S$) to 12.22 ns ($Zn_{0.8}Cd_{0.2}S/Co_3O_4$ sample), which reflected that the overall emission decay has been prohibited. For the photocatalytic material system, the efficiently restrained recombination of photo-generated electrons and holes results in a significantly prolonged lifetime, which will realize the provision of long-lived electrons for photocatalytic redox reactions.

To reveal the photocatalytic CO_2 redox process, diffuse reflectance infrared Fourier transform spectroscopy (DRIFTS) were used to identify the pivotal intermediates formed during the light-driven CO_2 photoreduction. For the optimal $Zn_{0.8}Cd_{0.2}S/Co_3O_4$ (CZC_50%) sample, absorbed CO_2 gas species (2338, 2357 cm^{-1}), chemical absorbed CO_2^-(1260, 1660 cm^{-1}), bicarbonates (HCO_3^-, 1430–1440 cm^{-1}), and bidentate carbonate (CO_3^{2-}, 1300–1324 cm^{-1}) appeared immediately after the reaction for 5 min (Figure 5e). These carbon species confirmed the absorption interaction between CO_2 molecules and the surface of the photocatalyst. As the reaction proceeds, the lower frequency at 1800–1875 cm^{-1} is assigned to a weak multi-bonded CO[47] and the augmented peak at 2142 cm^{-1} is attributed to the emerging crucial product of CO.[48,49] This gives rise to a high selectivity CO, reaching close to 95%. As the reaction proceeds, the characteristic peaks of absorbed CO_2, the other intermediates and representative CO product increase and then reach a steady state.

Based on the above electrochemical and in-situ DRIFTS results, the band structure and a possible photocatalytic redox reaction mechanism of $Zn_xCd_{1-x}S$ and Co_3O_4 have been proposed. As shown in Figure 5f and Figure S23 (Supporting Information), Co_3O_4 is a p-type semiconductor and the Fermi level is close to its VB position, while $Zn_xCd_{1-x}S$ is an n-type semiconductor and the Fermi level is near CB level.[50] Due to the potential difference between $Zn_xCd_{1-x}S$ and Co_3O_4, the electrons would transfer from $Zn_xCd_{1-x}S$ to Co_3O_4 and the holes would go in the reverse direction. In this case, it would cause the accumulation of negative charges on the surface of Co_3O_4 and positive holes on $Zn_xCd_{1-x}S$. However, in the heterojunction formation process, when the Fermi level of $Zn_xCd_{1-x}S$ and Co_3O_4 reached an equilibrium, an internal electric field was simultaneously built with the direction from $Zn_xCd_{1-x}S$ to Co_3O_4. As a result, the band structure of Co_3O_4 would rise up while $Zn_xCd_{1-x}S$ would decrease until an equilibrium state is reached.[51] Under the electric field, the electrons would migrate to $Zn_xCd_{1-x}S$ where the electrons redox reactions mainly occur, resulting in H_2 production or CO_2 reduction. Holes would transfer from $Zn_xCd_{1-x}S$ to Co_3O_4, and further be consumed by sacrificial agent or H_2O.

3. Conclusion

In summary, MOF-deriving porous Co_3O_4 host framework with $Zn_xCd_{1-x}S$ guest semiconductor hybrid photocatalyst is rationally prepared with continuous modulated electronic band structure and abounding heterojunctions for selective photocatalytic CO_2 conversion and H_2 production. The topological nanoassembly of guest semiconductor on the exterior and interior pores of the porous host matrix significantly create and expose multisites

© 2023 The Authors. Small published by Wiley-VCH GmbH

16136829, 0, Downloaded from https://onlinelibrary.wiley.com/doi/10.1002/smll.202301121, Wiley Online Library on [17/09/2023]. See the Terms and Conditions (https://onlinelibrary.wiley.com/terms-and-conditions) on Wiley Online Library for rules of use; OA articles are governed by the applicable Creative Commons License

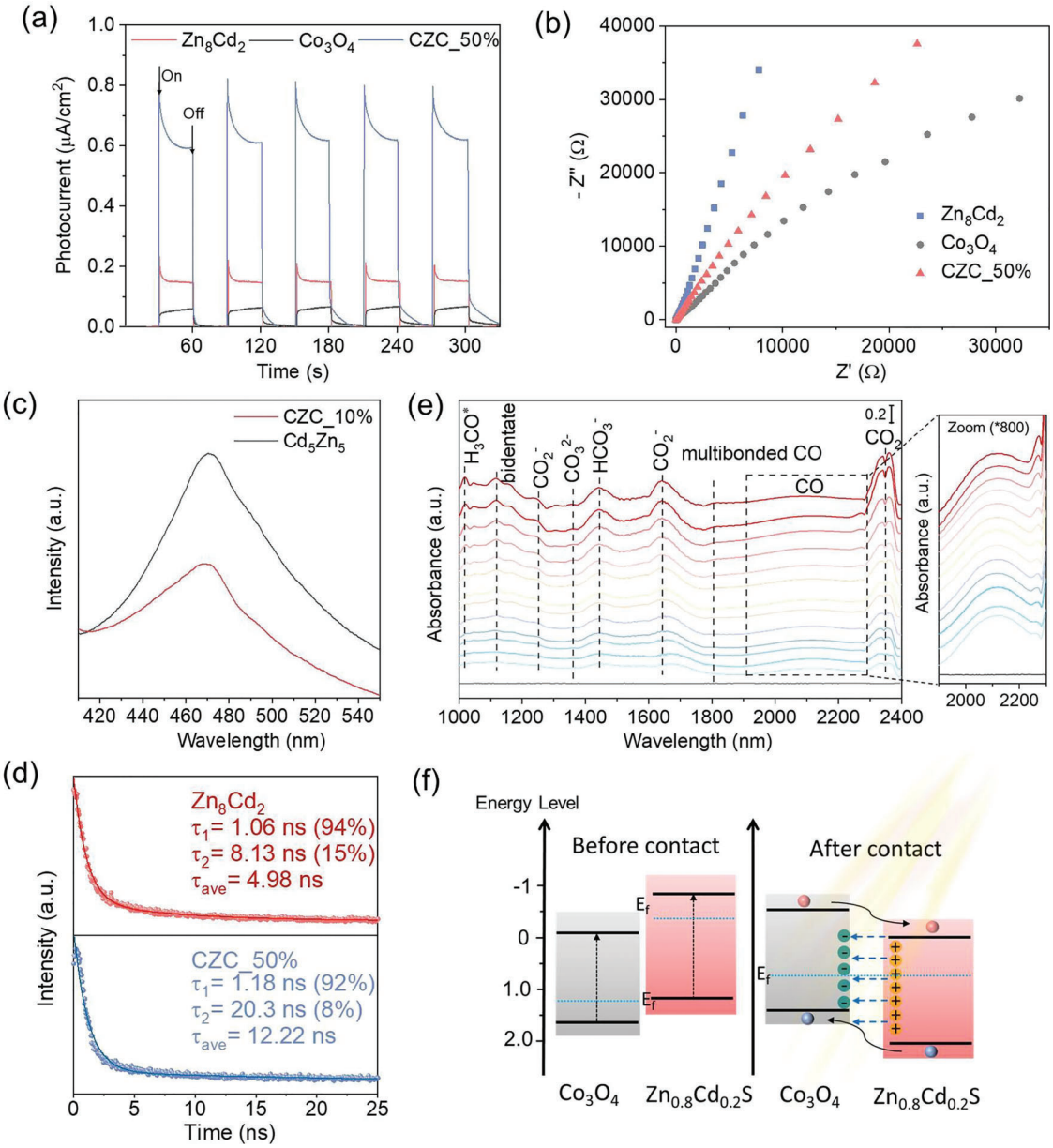

Figure 5. a) Photocurrent response, b) Nyquist plots of $Zn_{0.8}Cd_{0.2}S$, Co_3O_4, $Zn_{0.8}Cd_{0.2}S/Co_3O_4$ composites. c) Fluorescence spectra of $Zn_{0.5}Cd_{0.5}S$ and $Zn_{0.5}Cd_{0.5}S/Co_3O_4$ composites. d) Time-resolved transient photoluminescence (PL) decay spectra of $Zn_{0.8}Cd_{0.2}S$ and $Zn_{0.8}Cd_{0.2}S/Co_3O_4$ composites. e) Diffuse reflectance infrared Fourier transform spectroscopy of CZC_50% samples for photocatalytic CO_2 reduction under irradiation. f) Schematic diagram of band alignments over Co_3O_4 and $Zn_{0.8}Cd_{0.2}S$.

heterojunctions and thus contribute to efficient mass and charge transfer. The experimental characterizations and simulation results revealed that the introduction of a higher zinc concentration would controllably regulate the light absorption, promote an elevated conduction band position, better CO_2 absorption, and a lower energy barrier of specific reaction intermediates, thus realizing the reaction control toward photocatalytic CO_2 conversion. Furthermore, the Co_3O_4 framework, not only acts as the host support to load $Zn_xCd_{1-x}S$ guest nanoparticles but also promotes an enhanced charge transfer ability, serving as the hole-trapping sites to further enhance the photocatalytic activity of $Zn_xCd_{1-x}S$. This work provides some insight into the rational design of spontaneous assembly of nanoparticulate host–guest hybrid photocatalysts with spatially confined high-density heterojunctions, modulable band structure for selective solar conversion reactions.

Supporting Information

Supporting Information is available from the Wiley Online Library or from the author.

 © 2023 The Authors. Small published by Wiley-VCH GmbH

16136829, 0, Downloaded from https://onlinelibrary.wiley.com/doi/10.1002/smll.202301121, Wiley Online Library on [17/09/2023]. See the Terms and Conditions (https://onlinelibrary.wiley.com/terms-and-conditions) on Wiley Online Library for rules of use; OA articles are governed by the applicable Creative Commons License

Acknowledgements

The authors gratefully thank the financial support from the A*STAR under its 2019 AME IRG & YIRG Grant Calls, A2083c0059 and NUS postdoctoral fellowship R-263-000-F12-281, FRC MOE T1 project (A-0009184-00-00), and A*STAR LCERFI project (Award ID: U2102d2011, A-8000278-00-00). The authors also acknowledge the Synchrotron Light Research Institute (Public Organization), SLRI, for the assistance from the staff of beamline 1.1 W.

Conflict of Interest

The authors declare no conflict of interest.

Data Availability Statement

The data that support the findings of this study are available from the corresponding author upon reasonable request.

Keywords

CO_2 reduction, H_2 evolution, heterojunction, metal–organic-frameworks, photocatalysts

Received: February 8, 2023
Revised: May 19, 2023
Published online:

[1] J. Gong, C. Li, M. R. Wasielewski, *Chem. Soc. Rev.* **2019**, *48*, 1862.
[2] E. Kabir, P. Kumar, S. Kumar, A. A. Adelodun, K.-H. Kim, *Renewable Sustainable Energy Rev.* **2018**, *82*, 894.
[3] T. Ding, Y. Zhou, W. L. Ong, G. W. Ho, *Mater. Today* **2021**, *42*, 178.
[4] J. L. Field, T. L. Richard, E. A. H. Smithwick, H. Cai, M. S. Laser, D. S. LeBauer, S. P. Long, K. Paustian, Z. Qin, J. J. Sheehan, P. Smith, M. Q. Wang, L. R. Lynd, *Proc. Natl. Acad. Sci. USA* **2020**, *117*, 21968.
[5] S. Cheng, Z. Sun, K. H. Lim, T. Z. H. Gani, T. Zhang, Y. Wang, H. Yin, K. Liu, H. Guo, T. Du, L. Liu, G. K. Li, Z. Yin, S. Kawi, *Adv. Energy Mater.* **2022**, *12*, 2200389.
[6] J. Qi, W. Zhang, R. Cao, *Adv. Energy Mater.* **2018**, *8*, 1701620.
[7] T. Zhang, F. Meng, M. Gao, W. L. Ong, K. G. Haw, T. Ding, G. W. Ho, S. Kawi, *EcoMat* **2021**, *3*, e12152.
[8] W. L. Ong, Y.-F. Lim, J. L. Ting Ong, G. W. Ho, *J. Mater. Chem. A* **2015**, *3*, 6509.
[9] T. J. Wong, F. J. Lim, M. Gao, G. H. Lee, G. W. Ho, *Catal. Sci. Technol.* **2013**, *3*, 1086.
[10] S. Guo, X. Li, X. Ren, L. Yang, J. Zhu, B. Wei, *Adv. Funct. Mater.* **2018**, *28*, 1802567.
[11] Y. Shi, G. Zhan, H. Li, X. Wang, X. Liu, L. Shi, K. Wei, C. Ling, Z. Li, H. Wang, C. Mao, X. Liu, L. Zhang, *Adv. Mater.* **2021**, *33*, 2100143.
[12] S. Das, J. Perez-Ramirez, J. Gong, N. Dewangan, K. Hidajat, B. C. Gates, S. Kawi, *Chem. Soc. Rev.* **2020**, *49*, 2937.
[13] T. Zhang, T. Wang, F. Meng, M. Yang, S. Kawi, *J. Mater. Chem. C* **2022**, *10*, 5400.
[14] A. Goyal, G. Marcandalli, V. A. Mints, M. T. M. Koper, *J. Am. Chem. Soc.* **2020**, *142*, 4154.
[15] J. Fu, K. Jiang, X. Qiu, J. Yu, M. Liu, *Mater. Today* **2020**, *32*, 222.
[16] S. Ouyang, J. Ye, *J. Am. Chem. Soc.* **2011**, *133*, 7757.
[17] T. Ohno, L. Bai, T. Hisatomi, K. Maeda, K. Domen, *J. Am. Chem. Soc.* **2012**, *134*, 8254.
[18] H. Lin, B. Sun, H. Wang, Q. Ruan, Y. Geng, Y. Li, J. Wu, W. Wang, J. Liu, X. Wang, *Small* **2019**, *15*, 1804115.
[19] X. Yu, H. Su, J. Zou, Q. Liu, L. Wang, H. Tang, *Chinese J. Catal.* **2022**, *43*, 421.
[20] W.-N. Wang, C.-X. Huang, C.-Y. Zhang, M.-L. Zhao, J. Zhang, H.-J. Chen, Z.-B. Zha, T. Zhao, H.-S. Qian, *Appl. Catal. B* **2018**, *224*, 854.
[21] H. Huang, Z. Wang, B. Luo, P. Chen, T. Lin, M. Xiao, S. Wang, B. Dai, W. Wang, J. Kou, C. Lu, Z. Xu, L. Wang, *Nano Energy* **2020**, *69*, 104410.
[22] X. Zhao, J. Feng, J. Liu, W. Shi, G. Yang, G. C. Wang, P. Cheng, *Angew. Chem., Int. Ed. Engl.* **2018**, *57*, 9790.
[23] Y. Su, Z. Zhang, H. Liu, Y. Wang, *Appl. Catal. B* **2017**, *200*, 448.
[24] Y.-C. Chen, Y.-S. Huang, H. Huang, P.-J. Su, T.-P. Perng, L.-J. Chen, *Nano Energy* **2020**, *67*, 104225.
[25] S. Chandrasekaran, L. Yao, L. Deng, C. Bowen, Y. Zhang, S. Chen, Z. Lin, F. Peng, P. Zhang, *Chem. Soc. Rev.* **2019**, *48*, 4178.
[26] X. Wang, L. Yu, B. Y. Guan, S. Song, X. W. D. Lou, *Adv. Mater.* **2018**, *30*, 1801211.
[27] T. Wang, P. Wang, W. Zang, X. Li, D. Chen, Z. Kou, S. Mu, J. Wang, *Adv. Funct. Mater.* **2021**, *32*, 2107382.
[28] L. Huang, B. Li, B. Su, Z. Xiong, C. Zhang, Y. Hou, Z. Ding, S. Wang, *J. Mater. Chem. A* **2020**, *8*, 7177.
[29] R. Zeng, K. Lian, B. Su, L. Lu, J. Lin, D. Tang, S. Lin, X. Wang, *Angew. Chem., Int. Ed. Engl.* **2021**, *60*, 25055.
[30] Y. Su, D. Ao, H. Liu, Y. Wang, *J. Mater. Chem. A* **2017**, *5*, 8680.
[31] H. Hu, K. Zhang, G. Yan, L. Shi, B. Jia, H. Huang, Y. Zhang, X. Sun, T. Ma, *Chinese J. Catal.* **2022**, *43*, 2332.
[32] Z. Zhao, J. Bian, L. Zhao, H. Wu, S. Xu, L. Sun, Z. Li, Z. Zhang, L. Jing, *Chinese J. Catal.* **2022**, *43*, 1331.
[33] C. Shi, S. Ye, X. Wang, F. Meng, J. Liu, T. Yang, W. Zhang, J. Wei, N. Ta, G. Q. M. Lu, M. Hu, J. Liu, *Adv. Sci. (Weinh)* **2021**, *8*, 2001987.
[34] G. Yilmaz, T. Yang, K. J. H. Lim, S. W. Chee, L. Shen, U. Mirsaidov, M. Bosman, G. W. Ho, *EcoMat* **2022**, *5*, e12312.
[35] M. Li, S. Zhang, L. Li, J. Han, X. Zhu, Q. Ge, H. Wang, *ACS Sustainable Chem. Eng.* **2020**, *8*, 11465.
[36] L. Wang, J. Wan, Y. Zhao, N. Yang, D. Wang, *J. Am. Chem. Soc.* **2019**, *141*, 2238.
[37] C. Gao, Q. Meng, K. Zhao, H. Yin, D. Wang, J. Guo, S. Zhao, L. Chang, M. He, Q. Li, H. Zhao, X. Huang, Y. Gao, Z. Tang, *Adv. Mater.* **2016**, *28*, 6485.
[38] H. M. Chen, C. K. Chen, R.-S. Liu, C.-C. Wu, W.-S. Chang, K.-H. Chen, T.-S. Chan, J.-F. Lee, D. P. Tsai, *Adv. Energy Mater.* **2011**, *1*, 742.
[39] I. A. Pankin, O. E. Polozhentsev, M. A. Soldatov, A. L. Bugaev, A. Tsaturyan, K. A. Lomachenko, A. A. Guda, A. P. Budnyk, C. Lamberti, A. V. Soldatov, *J. Solid State Chem.* **2018**, *262*, 264.
[40] J. Zhang, L. Qi, J. Ran, J. Yu, S. Z. Qiao, *Adv. Energy Mater.* **2014**, *4*, 1301925.
[41] Q. Wang, G. Wang, J. Wang, J. Li, K. Wang, S. Zhou, Y. Su, *Adv. Sustain Syst.* **2022**, *7*, 2200027.
[42] X. Li, B. Kang, F. Dong, Z. Zhang, X. Luo, L. Han, J. Huang, Z. Feng, Z. Chen, J. Xu, B. Peng, Z. L. Wang, *Nano Energy* **2021**, *81*, 105671.
[43] N. Ojha, A. Bajpai, S. Kumar, *Catal. Sci. Technol.* **2019**, *9*, 4598.
[44] X.-K. Wang, J. Liu, L. Zhang, L.-Z. Dong, S.-L. Li, Y.-H. Kan, D.-S. Li, Y.-Q. Lan, *ACS Catal.* **2019**, *9*, 1726.
[45] X. Guo, C. Chang, G. Wang, X. Hao, Z. Jin, *Adv. Sustain. Syst.* **2022**, *7*, 2200189.
[46] T. Zhang, F. Meng, Y. Cheng, N. Dewangan, G. W. Ho, S. Kawi, *Appl. Catal. B* **2021**, *286*, 119853.
[47] P. Hongmanorom, J. Ashok, G. Zhang, Z. Bian, M. H. Wai, Y. Zeng, S. Xi, A. Borgna, S. Kawi, *Appl. Catal. B* **2021**, *282*, 119564.
[48] J. Wei, F. L. Meng, T. Li, T. Zhang, S. Xi, W. L. Ong, X. Q. Wang, X. Zhang, M. Bosman, G. W. Ho, *Adv. Funct. Mater.* **2021**, *32*, 2109693.
[49] X. Zhao, M. Xu, X. Song, W. Zhou, X. Liu, P. Huo, *Chinese J. Catal.* **2022**, *43*, 2625.
[50] Y. Zhang, Z. Jin, H. Yuan, G. Wang, B. Ma, *Appl. Surf. Sci.* **2018**, *462*, 213.
[51] S. Li, M. Cai, Y. Liu, J. Zhang, C. Wang, S. Zang, Y. Li, P. Zhang, X. Li, *Inorg. Chem. Front.* **2022**, *9*, 2479.

© 2023 The Authors. Small published by Wiley-VCH GmbH

16136829, 0, Downloaded from https://onlinelibrary.wiley.com/doi/10.1002/smll.202301121, Wiley Online Library on [17/09/2023]. See the Terms and Conditions (https://onlinelibrary.wiley.com/terms-and-conditions) on Wiley Online Library for rules of use; OA articles are governed by the applicable Creative Commons License